Research Article

Journal of Geophysical Research: Oceans
DOI 10.1002/2016JC012403

Thin ice and storms: sea ice deformation from buoy arrays deployed during N-ICE2015

Polona Itkin[1], Gunnar Spreen[1,2], Bin Cheng[5], Martin Doble[3], Fanny Girard-Ardhuin[4], Jari Haapala[5], Nick Hughes[6], Lars Kaleschke[7], Marcel Nicolaus[8], Jeremy Wilkinson[9]

Corresponding author: P. Itkin, Norwegian Polar Institute, Fram Centre, 9296 Troms, Norway. (Polona.Itkin@npolar.no)

[1]Norwegian Polar Institute, Tromsø,

Received: Aug 03, 2016; Revised: Jan 09, 2017; Accepted: Mar 13, 2017

Key Points.

- Two buoy arrays deployed in winter and spring 2015 showed very high sea ice deformation rates north of Svalbard.
- A storm event in early February irreversibly damaged the sea ice cover adjacent to the marginal ice zone.
- Single winter storm events, penetrating deep in the sea ice, can permanently precondition the sea ice cover for the subsequent melting.

Norway

[2]Institute of Environmental Physics,

University of Bremen, Bremen, Germany

[3]Polar Scientific Ltd

[4]IFREMER

[5]Finnish Meteorological Institute,

Helsinki, Finland

[6]Norwegian Meteorological Institute,

Tromsø, Norway

[7]Institute of Oceanography, University of

Hamburg, Hamburg, Germany

[8]Alfred-Wegener-Institut

Helmholtz-Zentrum für Polar- und

Meeresforschung, Bremerhaven, Germany

[9]British Antarctic Survey

Abstract.

Arctic sea ice has displayed significant thinning as well as an increase in drift speed in recent years. Taken together this suggests an associated rise in sea ice deformation rate. A winter and spring expedition to the sea ice covered region north of Svalbard the Norwegian young sea ICE 2015 expedition (N-ICE2015) - gave an opportunity to deploy extensive buoy arrays and to monitor the deformation of the first- and second-year ice now common in the majority of the Arctic Basin. During the 5-month long expedition, the ice cover underwent several strong deformation events, including a powerful storm in early February that damaged the ice cover irreversibly. The values of total deformation measured during N-ICE2015 exceed previously measured values in the Arctic Basin at similar scales: At 100 km scale, N-ICE2015 values averaged above 0.1 day^{-1}, compared to rates of 0.08 day^{-1} or less for previous buoy arrays. The exponent of the power law between the deformation length scale and total deformation developed over the season from 0.37 to 0.54 with an abrupt increase immediately after the early February storm, indicating a weakened ice cover with more free drift of the sea ice floes. Our results point to a general increase in deformation associated with the younger and thinner Arctic sea ice and to a potentially destructive role of winter storms.

1. Introduction

In addition to a remarkable shrinking and thinning [*AMAP*, 2013], the drift speed of the Arctic pack ice has increased, even though the wind forcing has remained of similar magnitude [*Rampal et al.*, 2009; *Spreen et al.*, 2011]. This has been ascribed to the reduced material strength of the thinner ice. The wind and ocean driven sea ice drift is not uniform and the differential motion causes the ice to break and deform in features like pressure ridges and leads. When the sea ice starts to melt in summer these features are the weak points along which the ice cover disintegrates [*Perovich et al.*, 2001; *Arntsen et al.*, 2015]. The summer sea ice extent can be additionally impacted by the storms and swell [*Asplin et al.*, 2012; *Zhang et al.*, 2013], but much of it is preconditioned by the sea ice dynamics during the cold season [e.g., *Kauker et al.*, 2009; *Kimura et al.*, 2013]. With higher drift speeds and weaker sea ice we expect more sea ice deformation that will have positive feedback on the sea ice mass balance, at least during winter, freezing conditions. During the melting season the stronger fractured sea ice that provides more surface for lateral melt and allows stronger wave penetration, can have an opposite effect, i.e., increased ice melting and thereby decrease in the ice volume.

Sea ice deformation depends strongly on its local sea ice conditions and the weather. This which makes a straightforward analysis difficult and statistical approaches must be used. Previous studies of deformation using a combination of satellite remote sensing data and buoy deployments [e.g., *Marsan et al.*, 2004; *Stern and Lindsay*, 2009; *Hutchings et al.*, 2011] described a power law relationship between deformation and the spatial scale on which it is measured. The law $D = aL^{-\beta}$, where D and L are deformation and length scale,

while a and β are constants indicates that deformation is spatially concentrated to small areas surrounded by vast undeformed regions. Deformation processes occur predominantly along long, narrow areas spanning up to few hundred kilometers, commonly termed linear kinematic features. If a small area contains an active deformation feature, the deformation value calculated for that area will be higher than for a larger area that contains the same feature, since the larger area contains a significant portion of undeformed sea ice. Knowing the β exponent of the power law we can statistically estimate the low spatial resolution values based on measurements of the high resolution total deformation and vice versa. This is essential for comparing, e.g., small scale in-situ measurements to larger scale satellite based products, or to the numerical model deformation estimates. Another use of β is that its value varies according to the degree of localization of deformation. An increase of β value in time means that the deformation attenuates at shorter spatial scales, which indicates reduced sea ice strength typical for warmer ice and free drift conditions. The value of β typically increases during the winter-summer transition [*Stern and Lindsay*, 2009] and depends on temperature [*Oikkonen et al.*, 2016] and distance from the ice edge [*Oikkonen et al.*, this issue].

The winter sea ice remains logistically hard to access and winter in-situ data are scarce. The sea ice covered region north of Svalbard is part of the Transpolar Drift system and is characterized by relatively high sea ice drift speeds, proximity to the ice edge, and lately also by the large fraction of first year sea ice, typically originating from the vast areas of Siberian shelf seas [*Renner et al.*, 2014]. The relative accessibility of this area during the winter makes it an ideal study region for the sea ice dynamics in the new Arctic. The region was studied during the Norwegian young sea ICE (N-ICE2015) expedition [*Granskog et al.*,

2016] in the first half of 2015. N-ICE2015 was a multidisciplinary expedition that collected data from the Arctic atmosphere, ocean, sea ice and ecosystem [*Cohen et al.*, this issue; *Meyer et al.*, this issue; *Provost et al.*, this issue; *Olsen et al.*, this issue]. The research work was based around the Norwegian Polar Institute research vessel Lance that was assisted to around 83°N by the Norwegian coastguard ice-breaker KV Svalbard on four occasions and left to drift passively southwards towards the ice edge.

The current study concentrates on buoy data from two of such southward drifts. A total of 42 buoys (Tables 2.1 and 1) were deployed in nested arrays at spacings of 5-100 km, separated into a winter deployment in January/February and a spring deployment in April/May. Instruments were placed on a mixture of first- and second-year ice that was characteristic for the region. The sea ice in the array was relatively thin with a modal thicknesses spanning between 0.9 m to 1.7 m and covered by thick snow cover with means between 30 and 50 cm for various ages of undeformed sea ice [*Rsel et al.*, 2016a, b]. The sea ice deformation on a smaller scale was simultaneously studied by analyzing ship radar images [*Oikkonen et al.*, this issue]. We compare our results to several previous studies which deployed buoy arrays (Figure 1) in late winter and spring in the 2000s: ACSYS in 2003 (Transpolar Drift north of Svalbard, 10 buoys deployed in April 2003), DAMOCLES in 2007 (North Pole region, 16 buoys deployed in April 2007) and SEDNA in 2007 (Beaufort Sea, 12 buoys deployed in March 2007). While the deployment times of these arrays overlap, the N-ICE2015 winter array starts considerably earlier in the season than these previous efforts, which allows new insights.

In this paper we present the sea ice buoy dataset collected during N-ICE2015, study the sea ice dynamics based on the dataset, explore the temporal development of the sea ice

deformation processes, connect the information to the previous studies and propose links for the found differences with the recent changes in the Arctic sea ice cover and climate.

2. Methods and Data

2.1. Buoy data

Winter and spring deployments both aimed to create multi-scale buoy arrays for the dynamics study described here and for other scientific aims. As such, a wide range of instrument types were used, though these were dominantly on-ice beacons that sank once their supporting ice floe disintegrated. In this paper we refer to these instruments as 'buoys'. All are listed in Tables 2.1 and 1. The buoy types included simple drifters - Compact Air-Launched Ice Beacon (CALIB), surface velocity profilers (SVP) and ice beacons drifters (IC) all produced by MetOcean, Halifax Canada, snow beacons (SNOW, produced by MetOcean), 4 types of sea Ice Mass balance Buoys (IMBs) including SIMBA units (SAMS Research Services Ltd (SRSL), Oban, Scotland, IMB-Bs (Bruncin, Zagreb, Croatia), an IMB (MetOcean) and a seasonal IMB-S (Cold Regions Research and Engineering Laboratory (CRREL), Hanover, USA), radiation buoys (Affordable Arctic Radiation drifter - AFAR, MetOcean), wave buoys (Bruncin), ridge IMB buoys (RIDGE, Oceanic Thermistor Buoy Model 908 produced by Oceanic Measurement, Sydney, Canada), and a sea ice stress buoy (STRESS, CRREL). Logistics for the two deployment groups were very different: The winter array was deployed during polar night with the assistance of KV Svalbard, snow machines and hauling on ski, which limited the possibilities of constructing a large and symmetric array; while the spring array was deployed from a helicopter and Lance, resulting in it being more symmetric with clearly distinguishable inner and outer rings. For both deployments the buoys were deployed over approximately 1 month

and had a relatively short lifetime of up to 3 months. Some buoys stopped functioning before the array was finished. For the drifters with flotation support such as the SVPs we take the first occurrence of a drift speed greater than 2 m/s as the point when the buoy was no longer drifting on ice. Buoys with the longest deployment duration also had the highest drift speeds, since velocities increased towards the ice edge.

The winter array drifted in south and south-east direction with some buoys traveling over 1000 km (Figure 2). The spring array drifted southwestwards, with a track length of almost 700 km. The distance is calculated based on the hourly positions of the buoys and does not take into account additional meandering between the measurements. Many buoys were deployed in co-located clusters, and neighboring buoys GPS locations were used in the event of a close-by buoys GPS failure, which happened for several IMBs. One buoy was selected from each cluster or pair of buoys for the deformation calculations. Positions from a total of 13 and 16 buoys were used to construct the sea ice deformation buoy array for the winter and spring deployment, respectively. All buoy positions and IMB data acquired during N-ICE2015 are publicly available at http://data.npolar.no [*Itkin et al.*, 2015] and partly also at http://www.meereisportal.de. The IMB data from N-ICE2015 is described and analyzed in a separate paper by *Provost et al.* [this issue].

2.2. Sea ice conditions and origin

To understand the age and origin of ice in the study region and to be able to compare to the sea ice cover conditions to the previous years, we tracked the ice back in time with a coarse-resolution sea ice drift from satellite observations. We used daily ice motion vectors based on ASCAT scatterometer and SSM/I radiometer data [*Girard-Ardhuin and Ezraty*, 2012] for the winter months and bridged the gap in ice drift data during the

Table 1. List of the buoys deployed as part of the winter buoy array during the N-ICE2015 expedition. Duration of the buoy deployment is estimated until end of data transmission or to the point when the drift speed exceeded 2 m/s. Distance is calculated based on the recorded positions and does not account for the motion in between.

name	type	deployment date	deployment location	total duration (days)	distance covered (km)	average speed (m/s)	IMEI
CALIB_2015a[a]	drifter	2015-01-28	N83.0902 E17.7636	45	721	0.5490	300234062447630
CALIB_2015b[a]	drifter	2015-01-21	N83.1588 E20.0232	53	889	0.5770	300234062440630
CALIB_2015d[a]	drifter	2015-01-17	N83.2120 E20.7078	56	888	0.5427	300234061362150
CALIB_2015e[a]	drifter	2015-02-10	N82.3630 E18.9038	32	534	0.5666	300234061369130
CALIB_2015f[a]	drifter	2015-01-20	N83.1762 E20.0984	0	2	0.1364	300234061269230
SNOW_2015a	snow buoy	2015-01-25	N83.0138 E19.8446	27	442	0.1895	300234062311650
SVP_2015a	drifter	2015-01-18	N83.2238 E21.0196	95	2109	0.2579	300234062447650
SVP_2015c[a]	drifter	2015-01-30	N83.0382 E16.7684	44	758	0.5953	300234011090780
SIMBA_2015a	IMB	2015-01-14	N83.2463 E21.6447	60	1014	0.1935	300234061263830
SIMBA_2015b*	IMB	2015-01-15	N83.0458 E21.9495	42	660	0.1815	300234062420090
SIMBA_2015e*	IMB	2015-01-26	N83.0472 E18.7160	3 (25)[b]	unknown	unknown	300234060695050
SIMBA_2015f*	IMB	2015-01-25	N83.0138 E19.8446	27	442	0.1895	300234011383170
SIMBA_2015g	IMB	2015-01-29	N83.0905 E17.0404	42	846	0.2322	300234060666760
WAVE_2015a*	wave buoy	2015-01-15	N83.1691 E21.3318	21	85	0.2116	300025010247350
WAVE_2015b	wave buoy	2015-01-16	N82.6767 E23.2338	39	620	0.1940	300025010343830
WAVE_2015c	wave buoy	2015-01-16	N82.3456 E24.8132	30	513	0.2081	300025010249350
WAVE_2015d	wave buoy	2015-01-16	N82.0115 E25.4361	15	182	0.1485	300025010340820
STRESS_2015a*	stress buoy	2015-01-25	N83.0138 E19.8446	27	442	0.1895	300034013532140
IMB_2015a	IMB	2015-01-18	N82.9843 E21.5213	42	660	0.1815	300025000000000

* Buoys not used for the sea ice deformation calculation.

[a] Buoys with 3-hourly GPS position.

[b] GPS antenna failed soon after deployment. Iridium position and data available for number of days in brackets.

Table 2. List of the buoys deployed as part of the spring buoy array during the N-ICE2015 expedition. Duration of the buoy deployment is estimated until end of data transmission or to the point when the drift speed exceeded 2 m/s. Distance is calculated based on the recorded positions and does not account for the motion in between.

name	type	deployment date	deployment location	total duration (days)	distance covered (km)	average speed (m/s)	IMEI
CALIB_2015c[a]	drifter	2015-04-21	N82.9660 E16.4936	43	486	0.3891	300234061371430
CALIB_2015g[a]	drifter	2015-04-21	N82.9242 E16.1952	46	594	0.4463	300234061369140
SNOW_2015d	snow buoy	2015-03-01	N82.9480 E26.4312	66	904	0.1582	300234062424060
SNOW_2015b	snow buoy	2015-04-23	N82.7944 E16.2662	46	613	0.1518	300234062311650
SNOW_2015c	snow buoy	2015-04-20	N83.1798 E16.3920	51	659	0.1470	300234062426060
SNOW_2015e	snow buoy	2015-04-21	N83.0042 E16.0852	49	654	0.1521	300234062426150
SVP_2015b	drifter	2015-04-20	N82.8952 E14.0812	44	569	0.1497	300234062442640
SVP_2015d[a]	drifter	2015-04-27	N82.4800 E14.1466	44	566	0.4394	300234010080470
SVP_2015e[a]	drifter	2015-04-20	N83.0500 E15.0496	51	695	0.4702	300234010084440
SVP_2015f[a]	drifter	2015-04-20	N83.0506 E15.0672	50	633	0.4342	300234011091510
AFAR_2015a	radiation buoy	2015-05-04	N82.0044 E11.5790	39	548	0.1589	300234062726310
AFAR_2015b	radiation buoy	2015-05-04	N82.0920 E13.0624	38	542	0.1620	300234062317630
AFAR_2015c	radiation buoy	2015-05-08	N81.5956 E10.1742	32	374	0.1333	300234062722280
SIMBA_2015c	IMB	2015-04-22	N82.8610 E16.5697	48	669	0.1587	300234061760870
SIMBA_2015d	IMB	2015-03-07	N83.1578 E23.7701	77	1562	0.2342	300234061762880
WAVE_2015e	wave buoy	2015-04-17	N83.0534 E13.3942	36	450	0.1512	300025010345830
WAVE_2015f	wave buoy	2015-04-17	N82.4555 E17.7205	39	620	0.1930	300025010241360
IMB-B_2015a*	IMB	2015-05-04	N82.0885 E13.0590	25	264	0.1277	300025010735970
IMB-B_2015b*	IMB	2015-05-08	N81.5660 E9.9498	22	240	0.1293	300025010738970
IMB-B_2015c*	IMB	2015-05-04	N82.0044 E11.5786	30	315	0.1541	300025010731970
RIDGE_2015a*	ridge IMB	2015-29-04	N82.0488 E13.4294	22	210	0.1129	300234061879260
RIDGE_2015b*	ridge IMB	2015-06-12	N80.7645 E12.0827	17	310	0.2116	300234061874260
IMB-S_2015a[b]*	seasonal IMB	2015-05-19	N82.2333 E10.3226	117	unknown	unknown	300234061666330
IC_2015a*	drifter	2015-04-21	N82.9 E16.7	52	unknown	unknown	Argos

* Buoys not used for the sea ice deformation calculation.

[a] Buoys with 3-hourly GPS position.

[b] Buoys with 6-hourly GPS position.

summer months by using an unpublished version of summer ASCAT/SSMIS ice drift data by the same provider. Ice was tracked back to its origin for the five years between 2011 and 2015 always starting on 15 March of each year at 82.5°N and 20°E (Figure 1). The ice drift at a given position is obtained from the 62.5 km large grid cell of the ASCAT/SSMI drift dataset covering that position. The previous days position is estimated from that drift vector and the procedure is repeated going back in time until either land or ice concentrations below 15% for more than one day are encountered. Due to the low resolution of the ice drift data and some gaps in the ice drift fields, especially during summer, the ice back-trajectory will diverge from the real trajectory and have some uncertainty. This approach is suitable to determine the sea-ice source region within an approximately 100 km radius. The back-tracking algorithm does not consider new ice growth, i.e., the presented trajectories represent the oldest ice for that region. It does not contain any information of the ice age composition and in addition to the oldest ice large fractions of younger ice can be present. The backtracking results show that between 2011 and 2015 sea ice in the region was typically a mixture of second year ice - mainly formed in the Laptev Sea, and first year ice (2011, 2012 and 2015) or exclusively first year ice formed in the northern Barents Sea (2013 and 2014). The in-situ observations confirmed presence of the older sea ice within the N-ICE2015 buoy arrays [*Granskog et al.*, this issue], while the ice pack was predominantly first year ice.

The older sea ice is typically thicker and stronger than first year ice. To explore the influence of the ice age on the sea ice dynamics we looked at the sea ice drift speed trends in the area north of Svalbard since 2002. We analyzed a higher spatial resolution sea ice drift (31.25 km) based on AMSR-E and AMSR2 passive microwave data available during

winter months [*Girard-Ardhuin and Ezraty*, 2012]. The results of this product with 3-day resolution (Figure 3) show that although the sea ice drift speed in the N-ICE2015 region is following an increasing trend since 2003, the speeds in 2015 were lower than during years with exclusively first year ice (2013 and 2014). This implies that our study provides a lower margin for the deformation rates during recent years in the area.

As an auxiliary dataset to interpret the sea ice drift and deformation time series from the N-ICE2015 arrays we estimated the distance to the ice edge from the navigational sea ice charts produced by the Norwegian Meteorological Institute. The charts were updated with near-daily frequency by visual analysis of Synthetic Aperture Radar (SAR) images. We calculated the shortest distance between the center of the array (Lance) and the inner edge of the ice class 'open water'. The distance between the buoy array and the ice edge started at just below 200 km and it was gradually decreasing towards 0 km for both arrays.

2.3. Deformation calculation

Deformation rates were calculated from triangles (Figure 2) formed between the buoys (numbered 1-3 in the equations below). Following *Hutchings et al.* [2012] Green's Theorem method was used to calculate the strain rates within the triangles defined by line integrals. For every buoy we projected its position at every time step to a geographical grid to obtain zonal and meridional coordinates (x,y). Velocities of a buoy (u,v) at a given time step were estimated based on the displacements from the position of the previous time step. Since triangles with very acute angles give inaccurate results, only triangles with all the corners larger than 15° were taken into the analysis. In contrast to the method used by *Hutchings et al.* [2011] we did not predefine or follow individual shapes, but we estimated

the strain rate components $\frac{\partial u}{\partial x}$, $\frac{\partial u}{\partial y}$, $\frac{\partial v}{\partial x}$ and $\frac{\partial v}{\partial y}$ for all possible triangles that satisfy the minimum angle criteria and with vertices arranged in a counter-clockwise order at every time step as:

$$\frac{\partial u}{\partial x} = \frac{1}{2A}\Big[(u_1+u_3)(y_1-y_3)+(u_1+u_2)(y_1-y_2)+(u_2+u_3)(y_2-y_3)\Big], \quad (1)$$

$$\frac{\partial u}{\partial y} = -\frac{1}{2A}\Big[(u_1+u_3)(x_1-x_3)+(u_1+u_2)(x_1-x_2)+(u_2+u_3)(x_2-x_3)\Big], \quad (2)$$

$$\frac{\partial v}{\partial x} = \frac{1}{2A}\Big[(v_1+v_3)(y_1-y_3)+(v_1+v_2)(y_1-y_2)+(v_2+v_3)(y_2-y_3)\Big], \quad (3)$$

$$\frac{\partial v}{\partial y} = -\frac{1}{2A}\Big[(v_1+v_3)(x_1-x_3)+(v_1+v_2)(x_1-x_2)+(v_2+v_3)(x_2-x_3)\Big], \quad (4)$$

where A is the triangle area. The divergence div is defined as:

$$div = \frac{\partial u}{\partial x} + \frac{\partial v}{\partial y} \quad (5)$$

and maximal shear rate shr as:

$$shr = \sqrt{\left(\frac{\partial u}{\partial x} - \frac{\partial v}{\partial y}\right)^2 + \left(\frac{\partial u}{dy} + \frac{\partial v}{\partial x}\right)^2}. \quad (6)$$

The GPS receivers were programmed to sample at every full hour, though some clock drift was evident for several buoys. We linearly interpolated (assuming constant drift speed and direction) the position of any such instruments to the full hour before using it in the calculations. Also whilst the majority of the N-ICE2015 buoys were providing GPS positions every hour, some were only sampling every 3 hours (Tables 2.1 and 1). To be able to use all the data we constructed the time series of deformation from the buoys with hourly data and then downscaled all the data to 3-hourly resolution to obtain as many

data points as possible for estimates of total deformation, defined as $D = \sqrt{div^2 + shr^2}$. The total deformation was used to assess the scaling law in sea ice deformation where

$$D \propto L^{-\beta} \tag{7}$$

and $L = \sqrt{A}$. For this task we did not bin the triangles in length scale L classes. Instead we fitted the function to all individual data points. This enables a more robust fit with narrower confidence bands.

The buoy producers have estimated the positioning error δ_x of stationary buoy to be around 25 m. For a moving platform δ_x increases and to add an extra error margin we used $\delta_x = 50m$. The velocity error can be estimated as $\delta_U = \frac{\sqrt{2}\delta_x}{T}$ [*Hutchings et al.*, 2012] that yields to 0.01 m/s. All the cases when a certain buoy was moving with a velocity lower than this were excluded from the analysis. According to *Hutchings et al.* [2012] the error of the deformation estimate becomes negligible when $A >> 8N^2\delta_x^2$, where N is the number of buoys in the polygon. Our smallest L is about 2 km, which means that if $\delta_x < 235m$ our deformation estimates has reasonable signal to noise ratio.

3. Sea ice deformation in connection to the storms and break-up events during N-ICE2015

The time series on Figure 4 show sea ice drift and deformation along with the most important forcing: wind and atmospheric temperatures, and consequences: distance to the sea ice edge and sea ice concentration. The temperature and wind data shown on the figure are observations from the meteorological mast at 2 and 10 m [*Cohen et al.*, this issue] positioned approximately in the center of the array. *Cohen et al.* [this issue] defined storms as events with wind speeds greater than 8 m/s for a duration of at least three hours

with breaks not longer than one hour. They divided the storms to minor and major, where only latter have a pressure decrease of more than 5 hPa in 6 hours. The divergence and shear in the time series are shown for two extreme scales of the array: the averages of the triangles with length scale smaller than 15 km and for the triangles larger than 60 km. Deformation at both scales is coherent and the peaks at the small scale are typically higher than at the large scale which is the consequence of the deformation localization. Moving averages with a 24 hour window were used to smooth the deformation time series and distinguish between predominantly divergent and convergent regimes.

The sea ice deformation measured by the N-ICE2015 buoys during the early part of the winter deployment was peaking during storms and during the wind direction changes (e.g. event on 27th January that could be a consequence of a distant storm passing), but was close to 0 between the events, indicating fast healing of the sea ice cover, similarly as described previously for the Arctic winter [*Hutchings et al.*, 2011]. The sea ice drift had a mean speed of 0.33 m/s, which is high compared to the January-May climatological drift speed of about 0.02 m/s in the whole Arctic Ocean (https://nsidc.org/data/docs/daac/nsidc0116_icemotion.gd.html) and had variable direction. As the buoys were in the Transpolar Drift current, and relatively close to the ice edge one would expect the drift speed to be higher than the Arctic as a whole, but the size of the difference was surprising. An unusually powerful storm between 3rd and 8th February that set the sea ice in even faster motion and opened large leads in the center of the buoy array [*Oikkonen et al.*, this issue]. The storm was perpetuated by an unusual extension of the polar vortex towards southern Greenland that displaced the jet stream associated with winds blowing along the Greenland coast northward, carrying cyclones with warm air and

moisture into the high Arctic [*Cohen et al.*, this issue]. Strong southerly winds followed by strong northerly winds compressed and then opened up the sea ice north of Svalbard. During this time the ice experienced a peak in convergence and shear followed by a strong peak in divergence (approximately 2 day^{-1}) and shear. The first peak indicated that the sea ice pressure was released by formation of pressure ridges in the shear zones. During the second peak the ice pack opened again and leads were formed. This is also reflected in the drop of the sea ice concentration towards 90%. The storm continued its trajectory further northeast of the N-ICE2015 region where it gradually dissipated [*Cohen et al.*, this issue] and likely caused similar sea ice deformation along its track. While there have been reports on storms and swell breaking up the summer sea ice in the central Arctic [*Asplin et al.*, 2012; *Simmonds and Rudeva*, 2012], powerful winter storms north of Svalbard are climatologically exceptional [*Cohen et al.*, this issue], but might occur at very high Arctic Oscillation index [*Simmonds and Keay*, 2009; *Cohen et al.*, this issue]. Storms are more common in the Nordic Seas in winter, as such these events can produce significant wave energy that can propagate northwards into the Arctic Ocean proper.

After the early-February storm the wind speed dropped, but the heavily deformed sea ice continued southward drift with a very fast speed of 0.86 m/s. The distance to the ice edge dropped below 50 km and the array was hit by another storm with two distinctive peaks of strong winds lasting from 15th to 16th and again from 17th to 21st February. The first peak compressed the ice pack (negative divergence values) by southerly winds, but at the beginning of the second peak winds turned southwards and the divergence gradually became positive. The ice pack stretched and finally broke up with a minor peak in shear on 18th February and a gradual increase in divergence. At this point the array was so

close to the ice edge that the breakup was possibly also assisted by swell propagating into the pack. After the break up sea ice in the array started to oscillate between divergent and convergent motion, sea ice concentration dropped below 80% and the IMBs in the array detected bottom melt and flooding of the ice floes [*Provost et al.*, this issue]. The array started to drift with high speeds (with mean at 0.93 m/s) associated with the free drift and majority of the buoys without flotation support were lost shortly afterwards (Table 2.1).

The N-ICE2015 array deployed in spring drifted predominantly south-west with a mean speed of 0.45 m/s. The deformation time series show only two major events, both connected to storms, none of which was as powerful as any of the major winter storms. The atmospheric circulation resembled an average situation with a smaller extension of the Polar vortex [*Cohen et al.*, this issue]. The atmospheric temperatures were still close to -20°C until a storm between 25th ad 27th April after which the temperatures were gradually increasing and finally approached positive values by the beginning of June. In contrast to the winter deployment, the spring deployment after April storm has visible oscillations in the divergence values (Figure 4). The oscillations have a sub-daily periodicity and are not visible in the moving averages with a window of 24 h. The oscillations could be a consequence of a more loose sea ice with lower sea ice internal strength due to high air temperatures or the reflection of the tides as the sea ice drifted over Yermak plateau where tidal amplitudes are higher than over deeper surrounding ocean [*Meyer et al.*, this issue]. Along with the rise of the atmospheric temperatures, mean sea ice temperatures measured by the IMBs in the array also increased from -20°C for the winter array [*Provost et al.*, this issue] to -10°C for the spring array [*Itkin et al.*, 2015].

The sea ice in the spring array broke up during the storm starting on 2nd June. The breakup is associated with a series of moderate peaks in shear and divergence. During and after the storm also the deformation values calculated for the large triangles between the buoys began to oscillate with a large amplitude. The divergence became predominantly positive, pointing to general disintegration of the sea ice cover and coinciding with the sea ice concentration drop below 80%. Drift velocity after the break up increased to 0.68 m/s. After 4th June sea ice drifted into the warm ocean surface waters and quickly started melting from the bottom and became nearly isothermal [*Itkin et al.*, 2015].

4. Spatial scaling relationships and comparison to the other datasets

Sea ice deformation measured on different spatial and temporal scales, locations and during different seasons cannot be compared directly. The power law in sea ice deformation (Equation 7) obtained through statistical analysis shows that the total deformation values (D) align along an exponential curve that decreases with increasing spatial scale (L). This makes it possible to compare the power law exponents (β) between different locations and seasons. β is essentially a measure of how well the deformations at low L transmits to the larger L - deformation localization. Scatter plots featuring the scaling relationship in deformation for the N-ICE2015 arrays (Figure 7 a, b and c) show a wide range of β. In the early part of winter deployment prior to the February storms β is lowest, 0.37. The exponent increases greatly during and after the storms - to 0.54 and it remains same large during the the spring deployment. Similar development is visible also directly in the deformation time series (Figure 4), where for the spring array small triangles consistently give larger average values than large triangles during peaks, while in the winter this only becomes clearly visible after the first February storm. The scatter plots also show a

similar development in the level of total deformation from winter to spring at short and long scales. For example, at the length scale of 10 km the mean total deformation for the winter pre-storm conditions was 0.3 day^{-1}, 0.5 day^{-1} for the winter post-storm and 0.4 day^{-1} for the spring conditions.

The N-ICE2015 β are comparable to the values obtained from other buoy deployments (Figure 7 d, e and f). *Hutchings et al.* [2011] previously calculated the exponent from an Arctic buoy array - SEDNA, deployed in the Beaufort sea in March 2007. To eliminate the methodological differences we recalculated the deformation rates for SEDNA using our procedures and additionally analyzed two other buoy arrays that have a length scale span large enough to construct a power law relationship: ACSYS from April 2003, covering nearly same region as N-ICE2015 and DAMOCLES from April 2007, covering the North pole region. For all three buoys arrays we assumed the same conservative positioning error as for the N-ICE2015 arrays ($\delta_x = 50m$). DAMOCLES and ACSYS buoy arrays are both missing small scale values, which could influence the steepness of the power law slope. All three earlier buoy arrays continue into the summer, but for this paper we analyzed data only with the time spans similar to N-ICE2015 arrays.

The earlier Arctic buoy array deployments (DAMOCLES, SEDNA and ACSYS) all show substantially lower rates of total deformation than N-ICE2015 arrays. While the mean total deformation at 100 km length scale exceeds 0.1 day^{-1} in all 3 cases for N-ICE2015 scatter plots (winter pre- and post-storm and spring), this is not the case for any of the earlier deployments. The elevated deformation rates were also confirmed at small length scales (50 m - 5 km) by the measurements based on the ship radar images [*Oikkonen et al.*, this issue]. β is variable between the experiments (0.35 for DAMOCLES, 0.41 for

ACSYS and 0.4 for SEDNA) and it increases southwards and towards the sea ice edge, but it remains lower than the winter port-storm and spring N-ICE2015 β values of 0.54 in all the cases. This suggests that the early winter (N-ICE2015 winter pre-storm) and high north (DAMOCLES) deformation values align along a power law with a β around 0.35, while late winter and spring datasets exhibit higher values between 0.4 and 0.54. The highest values were measured while the arrays were drifting though sea ice adjacent to the marginal ice zone.

5. Discussion

The sea ice deformation values, divergence and shear, peak during the storms. The direction of the sea ice drift, towards the ice edge or away from the ice edge, during the storm determines if the deformation will on average be divergent and produce leads with open water or not. The scatter plots of the sea ice drift direction and moving averages of divergence in Figure 5 show that storms (defined here as wind speed higher than 8 m/s, circles outlined in purple) that cause easterly or southerly drift - in the case of N-ICE2015 that coincides with directions towards the ice edge, resulted in more divergent motion, while other storms resulted predominantly in a convergent motion.

Figure 6 shows a scatter plot of divergence versus sea ice concentration (from AMSR2; www.seaice.uni-bremen.de; [*Spreen et al.*, 2008]). The data from the winter array shows a clear relationship between low sea ice concentrations - evidences for the presence of the leads, and positive divergence. A linear fit for the divergence and sea ice concentrations higher than 80% shows that the divergent motion is shortly followed by decrease in sea ice concentrations.

During the spring deployment there was only one storm causing clear divergent events (late April storm; Fig. 5) and strong wind events are more evenly distributed among sea ice drift direction with a frequency peak at already predominant south-west drift which in average resulted in convergent motion. If the data is representative of other years this suggests that in the N-ICE2015 region only powerful winter storms can cause a strong divergence and shear that opens up leads, which can be associated with a subsequent drop in ice concentration. In spring conditions, when there was no such powerful storm and when the sea ice cover has been previously broken up by the winter storms, this relationship breaks down.

Although the spring array deformation time series has only a few visible events and the sea ice drift speed was lower than for the winter array, the general level of the deformation and the power law exponent remain high despite low temperatures. The reason for this might be that the spring array was deployed on sea ice that was broken up during the winter storms upstream in the Transpolar Drift and was still drifting in the N-ICE2015 region. Besides the early February storm there was a similarly powerful storm also in mid-March during the second drift of Lance [*Cohen et al.*, this issue]. During that storm no buoy array was deployed and no deformation data are available. The spring array was deployed less than 100 km upstream of the ice floe on which a meteorological mast was installed during that previous drift. There is clear increase in the wind factor (ratio drift speed vs. wind speed) during the calm periods (times when wind speed remains below 8 m/s) before and after the early-February storm (Figure 8), i.e., the sea ice drifts faster for the same wind forcing after the storm than before the storm. This shows how the sea

ice cover never recovered after the early February storm or that it was again and further damaged during the mid-March storm.

The sea ice during N-ICE2015 had a modal thickness at 0.9 m for the first year and 1.5 m for the second year ice in the winter period, and 1.7 m in spring for both ice ages [*Rsel et al.*, 2016a, b]. This is noticeably thinner than the sea ice in which buoy arrays of SEDNA, DAMOCLES and ACSYS were deployed (approximately 2 m). Furthermore, the sharp rise of the N-ICE2015 late winter array β (0.54) that remained high throughout the N-ICE2015 spring deployment indicates the importance of the high latitude penetrating winter storms for the sea ice deformation scaling. This demonstrates that the scaling law exponent β varies in space and time, and can only be used to compare ice deformation observations, which were obtained under similar conditions but at different scales.

In the N-ICE2015 region β is exceptionally high, indicating close to free ice drift for large parts of late winter and spring 2015. During this period the wind was predominantly northerly, the sea ice was drifting towards the marginal ice zone and was not confined against any boundary. *Oikkonen et al.* [this issue] analyzed a simultaneous high resolution deformation dataset based on the ship radar images taken from Lance for a small area (15 by 15 km) in the center of the buoy array and found a gradual increase of β with decreasing distance to the ice edge. The strong increase in β and sea ice deformation overall between early and later winter can be associated with a strong storm event in the early February. All analyzed variables like β, divergence, shear and wind factor show a clear and irreversible change in their behavior after the initial ice break-up by this storm and the sea ice pack could not be consolidated again despite low air temperatures below -10° for the majority of the array drift until mid May. This shows that the timing of the

first winter storm that is penetrating deep into the ice cover can determine the sea ice dynamic behavior on a medium to large scale adjacent to the marginal ice zone for the rest of the winter and spring. Further data collection would be necessary to explore how such a storm would affect regions in the Central Arctic where pack ice is similarly thin and young as it was in the N-ICE region but more restricted by surrounding ice and land masses.

A faster drifting more dynamic ice cover, with, e.g., more leads opening up and higher wave amplitudes, is more susceptible to lateral melt when temperatures increase [*Asplin et al.*, 2012; *Perovich et al.*, 2001]. An early observation of a powerful storm such as the one in early February 2015 and the successive change in sea ice dynamics therefore yields potential predictability for the summer sea ice cover.

6. Conclusions

N-ICE2015 was a unique winter and spring five month long drift experiment in the sea ice North of Svalbard. The accompanying buoy arrays deployed to monitor the sea ice conditions and dynamics in a larger region were primarily influenced by the relatively thin sea ice cover [*Rsel et al.*, 2016a, b] and several exceptionally powerful winter storms [*Cohen et al.*, this issue]. The combination of both caused high winter sea ice deformation values that remained high even during spring, when the winds were less powerful. The sea ice in the region was likely still impacted by the previous winter storms that broke up the ice upstream of the Transpolar drift. Previous studies have shown that the power law for the scaling of sea ice deformation becomes steeper in summer [*Stern and Lindsay*, 2009]. Our results indicate that in the 'new' Arctic with now predominantly young and thin ice a powerful Arctic winter storm can have long lasting consequences for the sea ice

dynamics, at least for regions like the Northern Barents Sea or north of Svalbard, which are not confined by coastlines and allow free ice drift after a storm. Such a storm can cause steepening of the power law of deformation already in the winter and keep it high despite low atmospheric temperatures. Although storms experienced during N-ICE2015 are still unusual, another powerful storm affected the region already in December 2015 [*Boisvert et al.*, 2016] and a positive trend in moist intrusions [*Woods and Caballero*, 2016] suggests increased storm activity in this part of the Arctic in the future.

The elevated values of deformation during N-ICE2015 along with the increasing sea ice drift speed trend also show that the level of sea ice deformation in the Arctic likely have increased and will increase in the future if the ice thinning continues. This would not only contribute to reduced floe sizes, more lateral flooding, and hence stronger snow-ice formation [*Provost et al.*, this issue], but also to higher propagation of the ocean wave energy into the ice pack that causes further break ups and altogether facilities more lateral ice melt during summer, more open water and potentially more algal blooms and associated ecosystem shifts [*Assmy*, submitted; *Olsen et al.*, this issue] and would finally also influence the economic activities in the sea ice covered regions.

The N-ICE2015 winter buoy array deployment is the first extensive multidisciplinary buoy array deployed so early in the season in the Arctic and provides an extensive dataset that can be used not only for analysis of the sea ice dynamics and ice mass balance [*Provost et al.*, this issue], but also for the atmosphere and ocean surface properties.

Acknowledgments. We deeply thank the crew and scientists on board R/V Lance. There was a huge number of people to whom we are grateful for their help with the buoy deployments, among them Bengt Rotmo, Ottar Skog and Steinar Aksnes stand

out with their efforts during the winter deployment. We also thank the crew of the ice breaker KV Svalbard for assisting the travel of R/V Lance through the pack ice and deploying and recovering some of the buoys. The buoys itself were contributed by the Norwegian Polar Institute (through Centre for Ice, Climate and Ecosystems (ICE), Research Council of Norway project STASIS (221961/F20) and ICE-ARC programme from the European Union 7th Framework Programme, grant number 603887), University of Hamburg (through project DFG EXC177), Finnish Meteorological Institute, British Antarctic Survey, the Helmholtz infrastructure program FRAM of the Alfred-Wegener-Institut and Norwegian University of Science and Technology (NTNU). This work has been supported by the Norwegian Polar Institutes Centre for Ice, Climate and Ecosystems (ICE) through the N-ICE project. BC was funded by the Academy of Finland grant no. 283101. JH was funded by the Academy of Finland grant no. 279310. We are grateful to Jennifer Hutchings for valuable advises on the buoy data processing. We thank Norwegian Meteorological Institute for ice chart data and Bremen University for the ice concentration maps. N-ICE2015 acknowledges the in-kind contributions provided by other national and international projects and participating institutions, through personnel, equipment and other support. All the data used in this paper is published in the Norwegian Polar Institute database http://data.npolar.no and partly also at http://www.meereisportal.de (grant: REKLIM-2013-04).

References

AMAP (2013), *Arctic Climate Issues 2011: Changes in Arctic Snow, Water, Ice and Permafrost. SWIPA 2011 Overview Report.*, 97 pp., Arctic Monitoring and Assessment

Programme (AMAP).

Arntsen, A. E., A. J. Song, D. K. Perovich, and J. A. Richter-Menge (2015), Observations of the summer breakup of an arctic sea ice cover, *Geophysical Research Letters*, *42*(19), 8057–8063, doi:10.1002/2015GL065224, 2015GL065224.

Asplin, M. G., R. Galley, D. G. Barber, and S. Prinsenberg (2012), Fracture of summer perennial sea ice by ocean swell as a result of arctic storms, *Journal of Geophysical Research: Oceans*, *117*(C6), n/a–n/a, doi:10.1029/2011JC007221, c06025.

Assmy, P. (submitted), Arctic phytoplankton spring bloom beneath thick snow-covered sea ice, *Nature xx*.

Boisvert, L. N., A. A. Petty, and J. C. Stroeve (2016), The impact of the extreme winter 2015/16 arctic cyclone on the barentskara seas, *Monthly Weather Review*, *144*(11), 4279–4287, doi:10.1175/MWR-D-16-0234.1.

Cohen, L., S. Hudson, V. Walden, and M. Granskog (this issue), Meteorological conditons over arctic sea ice from winter through early summer during the norwegian young sea ice expedition (n-ice2015).

Doble, M. (this issue), Pack ice breakup by a winter storm a case study from the 2015 n-ice drift.

Girard-Ardhuin, F., and R. Ezraty (2012), Enhanced arctic sea ice drift estimation merging radiometer and scatterometer data, *IEEE Transactions on Geoscience and Remote Sensing*, *50*(7), 2639–2648.

Granskog, M., A. Rösel, P. A. Dodd, D. Divine, S. Gerland, T. onu Martma, and M. J. Leng (this issue), Snow contribution to first-year and second-year arctic sea ice mass balance north of svalbard.

Granskog, M. A., P. Assmy, S. Gerland, G. Spreen, H. Steen, and L. H. Smedsrud (2016), Arctic research on thin ice: Consequences of arctic sea ice loss, *Eos*, *97*, doi: 10.1029/2016EO044097.

Hutchings, J. K., A. Roberts, C. A. Geiger, and J. Richter-Menge (2011), Spatial and temporal characterization of sea-ice deformation, *Annals of Glaciology*, *52*(57), 360–368.

Hutchings, J. K., P. Heil, A. Steer, and W. D. Hibler (2012), Subsynoptic scale spatial variability of sea ice deformation in the western weddell sea during early summer, *Journal of Geophysical Research: Oceans*, *117*(C1), n/a–n/a, doi:10.1029/2011JC006961, c01002.

Itkin, P., G. Spreen, S. R. Hudson, B. Cheng, M. Doble, N. Sennechael, C. Provost, J. Haapala, M. Nicolaus, L. Kaleschke, and J. Wilkinson (2015), N-ice2015 buoy data, doi:10.21334/npolar.2015.6ed9a8ca.

Kauker, F., T. Kaminski, M. Karcher, R. Giering, R. Gerdes, and M. Vobeck (2009), Adjoint analysis of the 2007 all time arctic sea-ice minimum, *Geophysical Research Letters*, *36*(3), n/a–n/a, doi:10.1029/2008GL036323, l03707.

Kimura, N., A. Nishimura, Y. Tanaka, and H. Yamaguchi (2013), Influence of winter sea-ice motion on summer ice cover in the arctic, *Polar Research*, *32*(0), doi: 10.3402/polar.v32i0.20193.

Marsan, D., H. Stern, R. Lindsay, and J. Weiss (2004), Scale dependence and localization of the deformation of arctic sea ice, *Phys. Rev. Lett.*, *93*, 178,501, doi: 10.1103/PhysRevLett.93.178501.

Meyer, A., A. Sundfjord, I. Fer, C. Provost, N. V. Robineau, Z. Koenig, I. Onarheim, P. Dodd, P. Duarte, H. Kauko, and L. H. Smedsrud (this issue), Winter to summer hydrographic and current observations in the arctic north of svalbard.

Oikkonen, A., J. Haapala, M. Lensu, and J. Karvonen (2016), Sea ice drift and deformation in the coastal boundary zone, *Geophysical Research Letters*, *43*(19), 10,303–10,310, doi: 10.1002/2016GL069632, 2016GL069632.

Oikkonen, A., J. Haapala, M. Lensu, J. Karvonen, and P. Itkin (this issue), Small scale sea ice deformation during n-ice2015: From compact pack ice to marginal ice zone.

Olsen, L. M., S. R. Laney, P. Duarte, H. M. Kauko, M. F. Mndez, C. J. Mundy, A. Rsel, A. Meyer, P. Itkin, L. Cohen, I. Peeken, A. Tatarek, J. Wiktor, H. Hop, and P. Assmy (this issue), The role of multiyear ice in seeding ice algae blooms in arctic pack ice.

Perovich, D. K., J. A. Richter-Menge, and W. B. Tucker (2001), Seasonal changes in arctic sea-ice morphology, *Annals of Glaciology*, *33*(1), 171–176.

Provost, C., N. Sennéchel, J. Miguet, P. Itkin, A. Rösel, K. Zoé, V. Nicolas, and G. M. A (this issue), Observations of snow-ice formation in a thinner arctic sea ice regime during the n-ice2015 campaign: influence of basal ice melt and storms.

Rampal, P., J. Weiss, and D. Marsan (2009), Positive trend in the mean speed and deformation rate of arctic sea ice, 19792007, *Journal of Geophysical Research: Oceans*, *114*(C5), n/a–n/a, doi:10.1029/2008JC005066, c05013.

Renner, A. H. H., S. Gerland, C. Haas, G. Spreen, J. F. Beckers, E. Hansen, M. Nicolaus, and H. Goodwin (2014), Evidence of arctic sea ice thinning from direct observations, *Geophysical Research Letters*, *41*(14), 5029–5036, doi:10.1002/2014GL060369.

Rösel, A., P. Itkin, J. King, D. Divine, S. Gerland, and T. Krumpen (this issue), Winter and spring development of sea-ice and snow thickness distributions north of svalbard observed during n-ice2015.

Rsel, A., D. Divine, J. A. King, M. Nicolaus, G. Spreen, P. Itkin, C. M. Polashenski, G. E. Liston, se Ervik, M. Espeseth, A. Gierisch, J. Haapala, N. Maa, A. Oikkonen, A. Orsi, A. Shestov, C. Wang, S. Gerland, and M. A. Granskog (2016a), N-ice2015 total (snow and ice) thickness data from em31, doi:10.21334/npolar.2016.70352512.

Rsel, A., C. M. Polashenski, G. E. Liston, J. A. King, M. Nicolaus, J.-C. Gallet, D. Divine, P. Itkin, G. Spreen, se Ervik, M. Espeseth, A. Gierisch, J. Haapala, N. Maa, A. Oikkonen, A. Orsi, A. Shestov, C. Wang, S. Gerland, and M. A. Granskog (2016b), N-ice2015 snow depth data with magna probe, doi:10.21334/npolar.2016.3d72756d.

Simmonds, I., and K. Keay (2009), Extraordinary september arctic sea ice reductions and their relationships with storm behavior over 19792008, *Geophysical Research Letters*, *36*(19), n/a–n/a, doi:10.1029/2009GL039810, l19715.

Simmonds, I., and I. Rudeva (2012), The great arctic cyclone of august 2012, *Geophysical Research Letters*, *39*(23), n/a–n/a, doi:10.1029/2012GL054259, l23709.

Spreen, G., L. Kaleschke, and G. Heygster (2008), Sea ice remote sensing using amsr-e 89-ghz channels, *Journal of Geophysical Research: Oceans*, *113*(C2), n/a–n/a, doi: 10.1029/2005JC003384, c02S03.

Spreen, G., R. Kwok, and D. Menemenlis (2011), Trends in arctic sea ice drift and role of wind forcing: 19922009, *Geophysical Research Letters*, *38*(19), n/a–n/a, doi: 10.1029/2011GL048970, l19501.

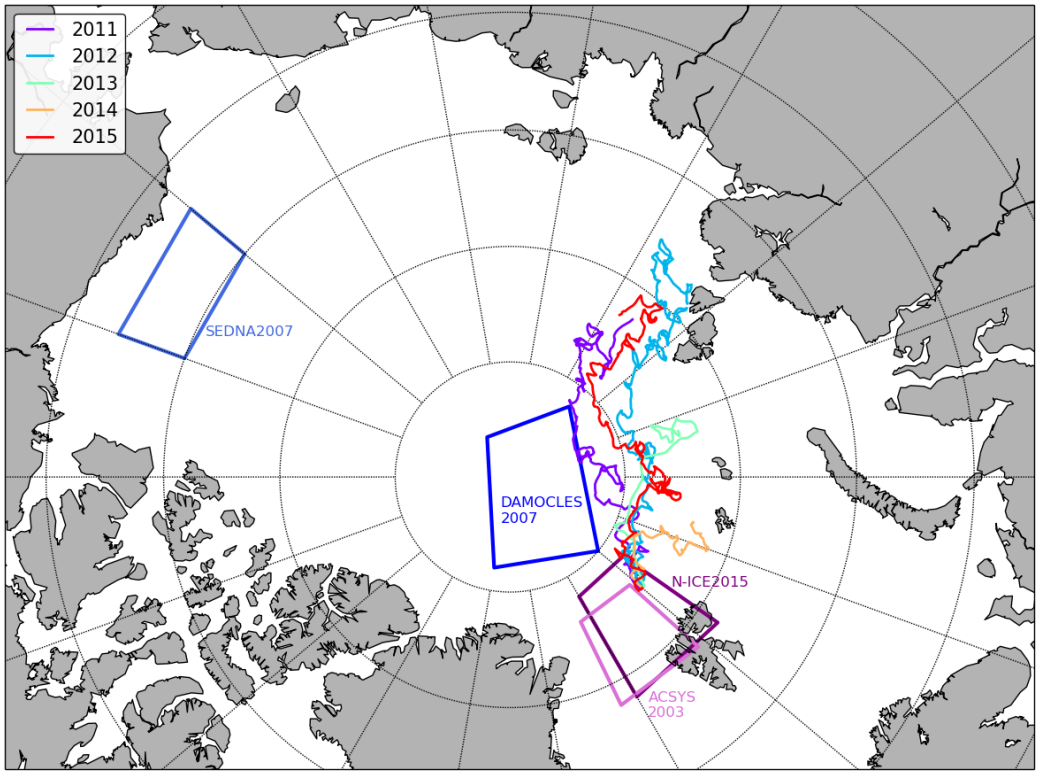

Figure 1. Back trajectories of the sea ice in the N-ICE2015 region for recent years (2011-2015) show the typical origin of the ice in that region. Regions of buoy arrays used in this study (N-ICE2015, SEDNA2007, ACSYS2003 and DAMOCLES2007) are shown as boxes.

Stern, H. L., and R. W. Lindsay (2009), Spatial scaling of arctic sea ice deformation, *Journal of Geophysical Research: Oceans*, *114*(C10), n/a–n/a, doi:10.1029/2009JC005380, c10017.

Woods, C., and R. Caballero (2016), The role of moist intrusions in winter arctic warming and sea ice decline, *Journal of Climate*, *29*(12), 4473–4485, doi:10.1175/JCLI-D-15-0773.1.

Zhang, J., R. Lindsay, A. Schweiger, and M. Steele (2013), The impact of an intense summer cyclone on 2012 arctic sea ice retreat, *Geophysical Research Letters*, *40*(4), 720–726, doi:10.1002/grl.50190.

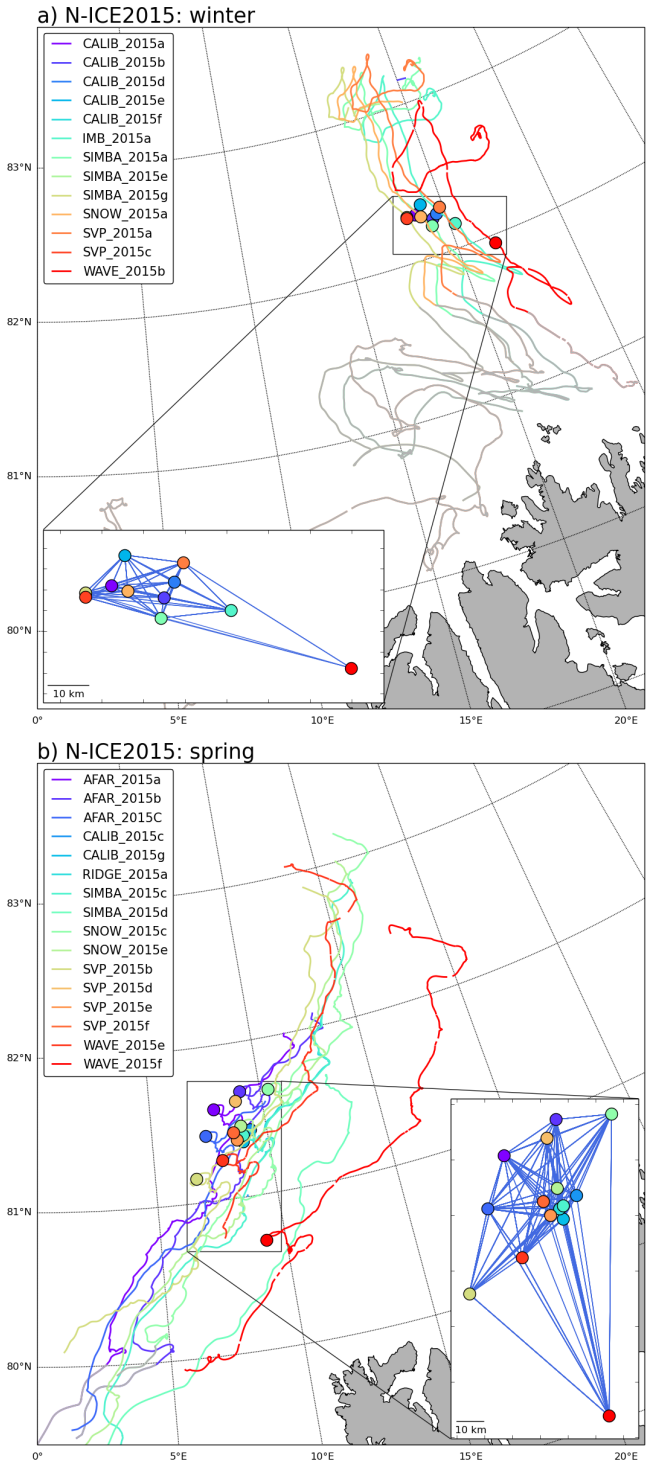

Figure 2. Buoy drift tracks for the winter (top) and spring (bottom) deployment. Only the buoys that were used for the deformation calculations are shown. The position of the buoys on 2nd February 2015 and 15th May 2015 is depicted by circles. By those dates all the buoys were deployed, but some had already ceased transmission. The triangles used for the deformation calculation are outlined by blue lines in the magnified map of the array. The buoy tracks after the break up are shaded in gray.

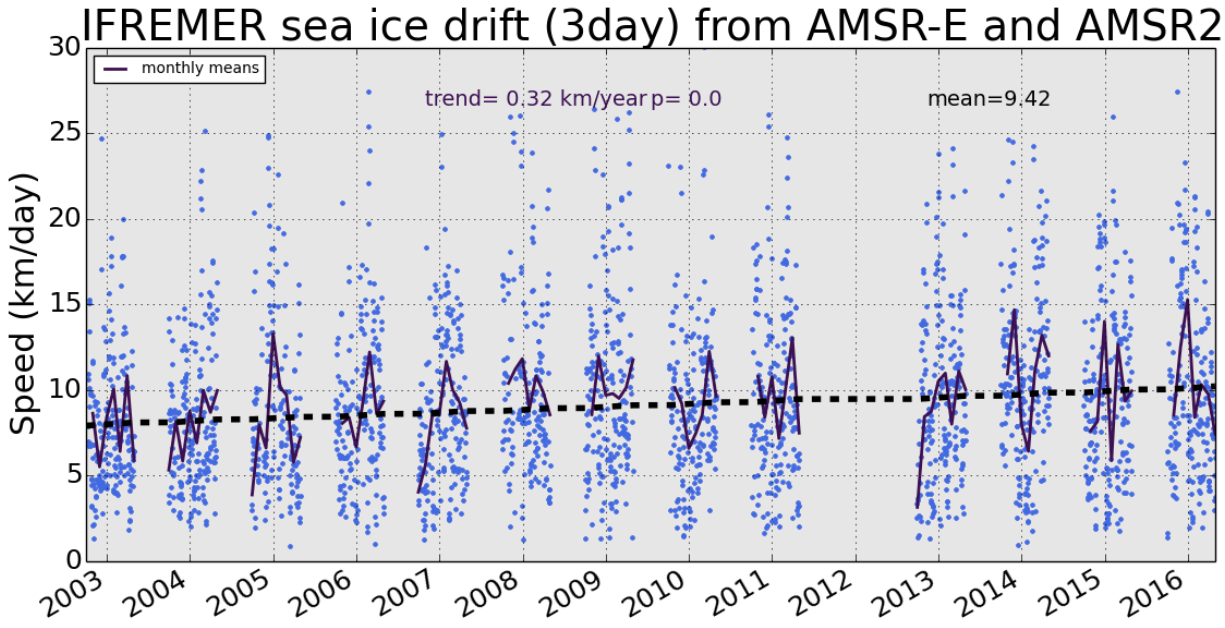

Figure 3. Time series of sea ice drift speeds, with monthly means and overall trend, in the N-ICE2015 region during winter (October-April) for the period 2003 to 2016.

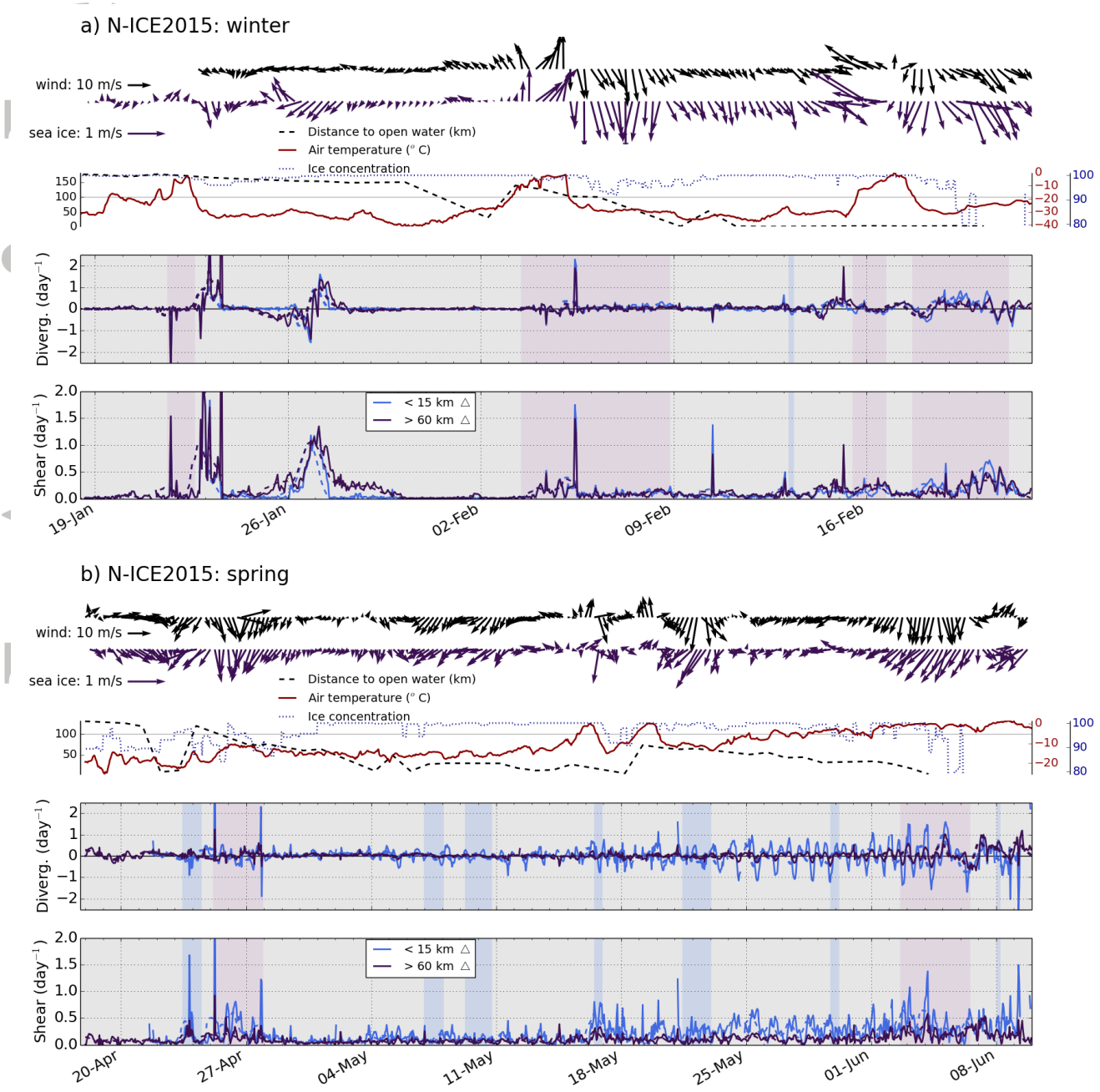

Figure 4. Mean sea ice drift, wind speed, distance from the open water, sea ice concentration, air temperature, divergence and shear during the winter (top) and spring (bottom) deployment. Areas shaded in purple and blue are major and minor storms. Sea ice drift is the average of all the buoys in the array and the wind data are from the meteorological mast in the center of the array. On the divergence and shear plots solid blue line is the average calculated for the small scale triangles (length scale smaller than 15 km) and solid purple lines are the averages for the big triangles (length scale greater than 60 km). Dashed lines are the running means with 24 h averaging window.

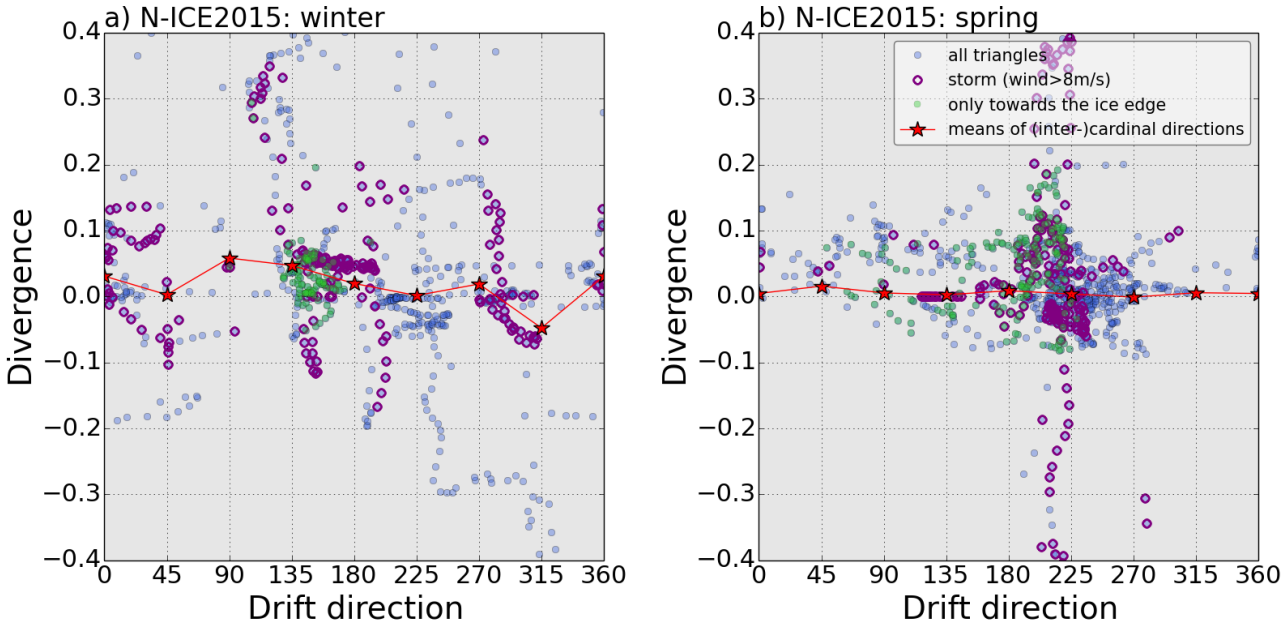

Figure 5. Scatter plots of sea ice divergence and sea ice drift angle; 0/360 is towards the north. All data points are plotted as blue circles. Storms - occasions where wind speed exceeds 8 m/s are outlined in purple. Data points where the sea ice moves towards the ice edge are overlayed by green circles. Here towards ice edge direction is sea ice drifting inside a 25° envelope around the shortest distance line from the array center to the open water. The average divergence of the inter-cardinal directions (N, NE, E, SE, S, SW, W and NW) are calculated for the storm events and depicted as red stars.

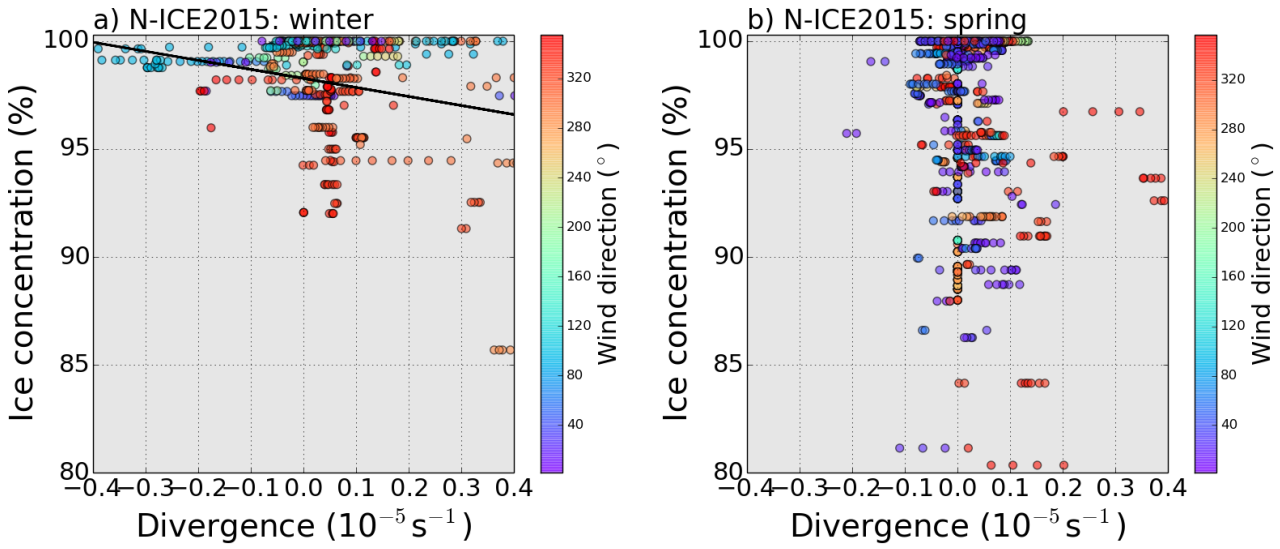

Figure 6. Scatter plots of sea ice divergence (moving averages over 24 hours) vs. ice concentration of the sea ice drift with the 2nd order polynomial fit for the sea ice concentrations lower than 100% and higher than 80%. Color of the markers is the wind direction.

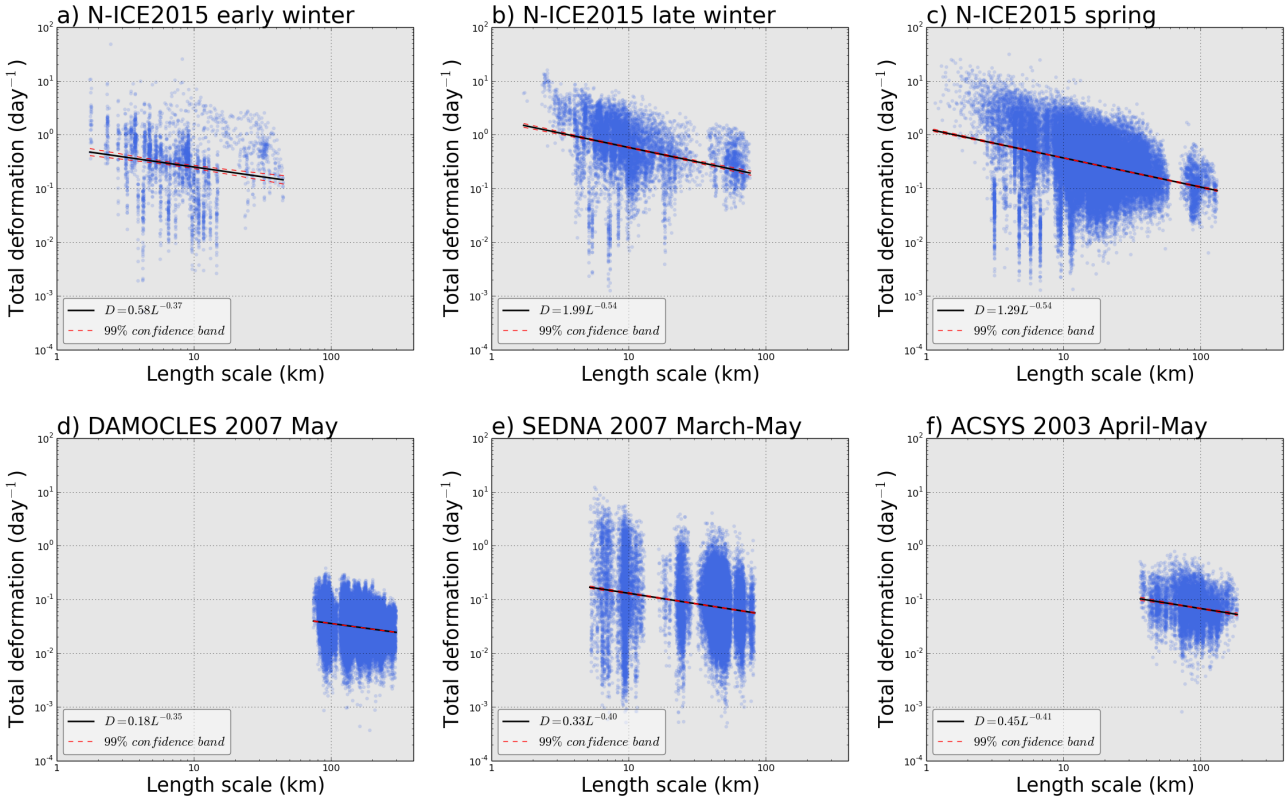

Figure 7. Scatter plots of length scale and total deformation for N-ICE2015 (a- winter before the storm, b - after the storm and c - spring), d - DAMOCLES 2007, e - SEDNA 2007 and f - ACSYS 2003. The exponential fit to the data is depicted with the black line that follows the power law. Note the logarithmic scale on both axis. Refer to Fig. 1 for locations of the array deployments.

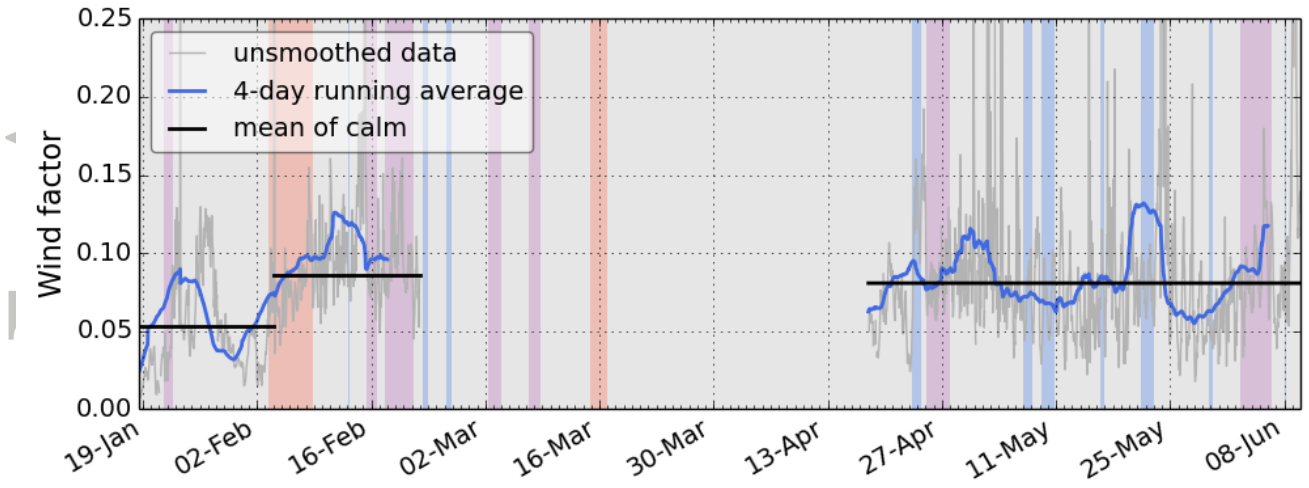

Figure 8. Time series of wind factor (drift speed/wind speed). Major and minor storms are highlighted by purple and blue shading. Most powerful storms (wind speed peak above 19 m/s and high maximum rate in air pressure decrease) are highlighted in orange.